Ultrafast transient increase of the oxygen octahedra rotation in a perovskite -Supplementary Information-

M. Porer,[1,*] M. Fechner,[2] M. Kubli,[3] M. J. Neugebauer,[3] S. Parchenko,[1] V. Esposito,[4] A. Narayan,[5] N. A. Spaldin,[5] R. Huber,[6] M. Radovic,[1] E. M. Bothschafter,[1] J. M. Glownia,[7] T. Sato,[7] S. Song,[7] S. L. Johnson,[3,4] and U. Staub[1,†]

[1]*Swiss Light Source, Paul Scherrer Institute, 5232 Villigen-PSI, Switzerland*

[2]*Max Planck Institute for the Structure and Dynamics of Matter, CFEL, 22761 Hamburg, Germany*

[3]*Institute for Quantum Electronics, ETH Zürich, 8093 Zürich, Switzerland*

[4]*SwissFEL, Paul Scherrer Institute, 5232 Villigen-PSI, Switzerland*

[5]*Materials Theory, ETH Zürich, 8093 Zürich, Switzerland*

[6]*Department of Physics, University of Regensburg, 93040 Regensburg, Germany*

[7]*LCLS, SLAC National Accelerator Laboratory, Menlo Park, California 94025, USA*

(Dated: May 6, 2019)

* Michael@Porer.org

† Urs.Staub@psi.ch

Time-resolved X-ray diffraction experiments

In the time resolved X-ray measurements performed at the XPP endstation of LCLS the sample surface was set to vertical. An X-ray photon energy of 9.5 keV with an X-ray pulse duration of 50 fs was used to probe the X-ray reflections at a repetition rate of 120 Hz. The incoming angle of the X-rays and the optical pump beam in respect to the sample surface was set to 5° and 5.5°, respectively. The X-ray beam diameter perpendicular to the beam axis was set to 50 μm (FWHM) at the sample position. For all excitation conditions, the spot size of the excitation laser beam was larger by more than a factor of two at the sample position. We recorded the intensity of the diffracted X-ray pulses using a CSPAD-140k area detector [1]. The intensity and position monitor (IPM) provided at XPP was used to record the intensity of the incident X-ray shots for filtering of shots with low intensity and intensity normalization. The spectral-encoding based timing tool [2] of the XPP endstation was used to determine the timing jitter between pump and probe pulses. This timing information was used to sort and bin the data into 50 fs wide time windows. We estimate the absorbed fluence within the $EuTiO_3$ film from the dielectric functions of $EuTiO_3$ and the $SrTiO_3$ substrate [3, 4] via an optical transfer-matrix method [5].

Structural AFD transition of the $EuTiO_3$ thin films in the quasi static case

For static characterization of the antiferrodistortive transition in our 40 nm thin film of $EuTiO_3$ we measured the intensity of a typical AFD induced superlattice reflection as a function of temperature (Materials Science Beamline X04SA, Swiss Light Source). Figure S1 shows the normalized peak intensity of the rocking curve (see Fig. 1b). The scattering intensity I is proportional to φ^2 [6]. We extrapolate a critical temperature for the antiferrodistortive transition of $T_c \approx 650\,\mathrm{K}$ by linear extrapolation of $\sqrt{I}$, which would represent a mean field behaviour. The behaviour is indicative for a distribution of transition temperatures which might relate directly to the significant damping observed in the soft mode modulation (Figure 1c of the main text).

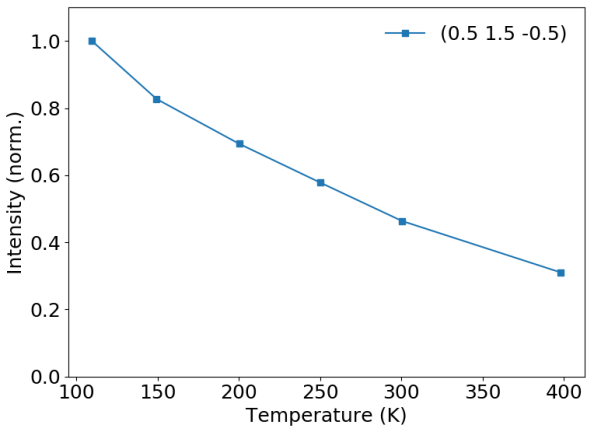

FIG. S1. Peak reflection intensity of a representative superlattice reflection (1/2 3/2 -1/2) as a function of temperature in thermal equilibrium normalized to its peak intensity at 115K. The line is a guide to the eyes.

Ultrafast dynamics of different AFD-induced superlattice reflections and temperature dependence of the dynamics

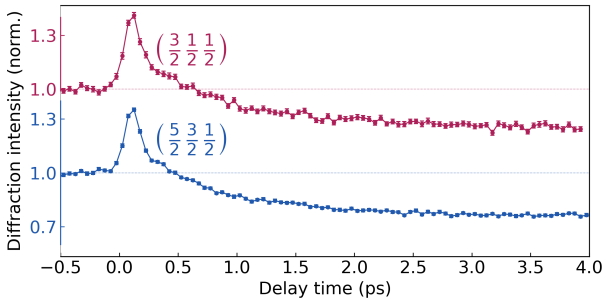

FIG. S2. Dynamics of two different-AFD induced superlattice reflections measured at $T = 120\,\mathrm{K}$. The pump photon energy is set to 3.1 eV and the absorbed fluence is $3.66\,\mathrm{mJ/cm^2}$. The lines are guides to the eyes.

In order to verify that the transient superlattice scattering intensity represents the dynamics of the octahedral rotation angle and not the Debye-Waller-Factor, we collected time traces of superlattice reflections that have significantly different X-ray momentum transfers **q** under similar excitation conditions (Figure S2). The similarity of the curves identifies changes of the octahedral rotation angle φ as the underlying structural dynamics and excludes a significant influence of the Debye-Waller factor, as discussed in the main text.

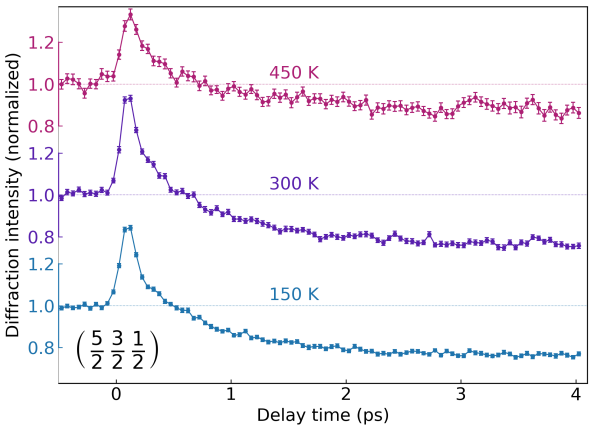

FIG. S3. Dynamics of the AFD induced superlattice reflection intensity for several temperatures. The photon energy of the exciting pulses is 3.1 eV and the absorbed fluence is 3.66 mJ/cm^2. The lines are guides to the eyes.

As we show in Figure S3, the initial lattice temperature does not significantly influence the photoinduced structural dynamics. We note that the sample position was re-optimized between acquisition of the curves at T = 150 K and T = 300 K to compensate for long time drifts.

DFT calculations

Density functional theory (DFT) calculations for $EuTiO_3$ are performed in an all-electron full-potential linearised augmented-plane wave approach as implemented in the Elk code [7] (version 4.3.6).

As approximation for the exchange-correlation functional we apply a generalized gradient approach plus U (GGA+U). Specifically, we use the PBEsol [8] GGA parameterization and apply a $U = 6.2\,\mathrm{eV}$ and $J = 1\,\mathrm{eV}$, such that the $4f$ Eu-states are energetically positioned between the valence and conduction states of O and Ti, respectively [9]. The muffin tin radii for Eu, Ti and O are set to 1.3 Å, 0.9 Å and 0.75 Å. We used a basis set of $l_{max_{\mathrm{APW}}} = 10$, $8\times8\times6$ k-point sampling of the Brillouin zone and took the product of the average muffin tin radius and the maximum reciprocal lattice vector to be 8.5. Further numerical parameters and convergence criteria (Δ for potential: $0.1\cdot10^{-6}\,E_\mathrm{h}$; Δ for total energy $0.1\cdot10^{-4}\,E_\mathrm{h}$) are adjusted according to the high-quality ('`highq .true.`') settings within the *elk* code.

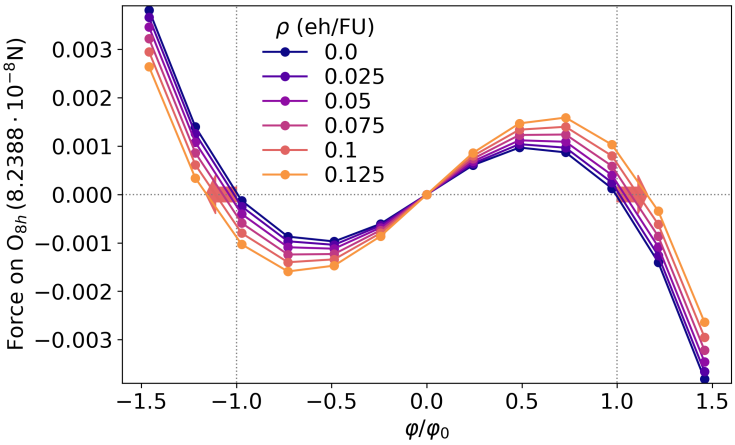

FIG. S4. Force on a individual Oxygen $8h$ site along the AFD soft-mode direction as a function of the static rotation amplitude φ and the eh-doping. Arrows indicate the shift of φ for zero force with increasing ρ.

We perform all DFT calculations on the distorted $EuTiO_3$ unit cell with space-group $I4/mcm$ (140). We set the lattice constants to the experimental values of $a = b = 5.52$ Å and $c = 7.80$ Å. Note that all computations assume the magnetization of the Eu atoms to be of G-type antiferromagnetic order. The local moment on the Eu sites is found to be $6.9\mu_\mathrm{b}$. The choice of the magnetic ground state is expected to have negligible influence on the AFD soft mode potential [10].

To simulate the situation of photodoping we constrained a number of electrons to the conduction band and the same number of holes to the valence band imposing two separate chemical potentials for electrons and holes, [11, 12]. These are reevaluated in each iteration of the self-consistency loop. We model the electronic excess energy (i.e. the energy separation of electrons and holes in addition to the band gap energy) via the temperature of the Fermidistribution of electrons and holes that defines the occupations of the electronic levels. To obtain the double-well potential of the AFD soft mode, we freeze the octahedral rotation angle φ at a series of values and calculate the atomic forces within the unit cell. In Figure S4 we show the resulting total force (which points solely along the direction of the AFD distortion) on one oxygen 8h site involved in the rotation. We parametrize the force with a polynomial of the form

$$F_O(\varphi, \rho) = a(\rho) \cdot \varphi + b(\rho) \cdot \varphi^3 \tag{1}$$

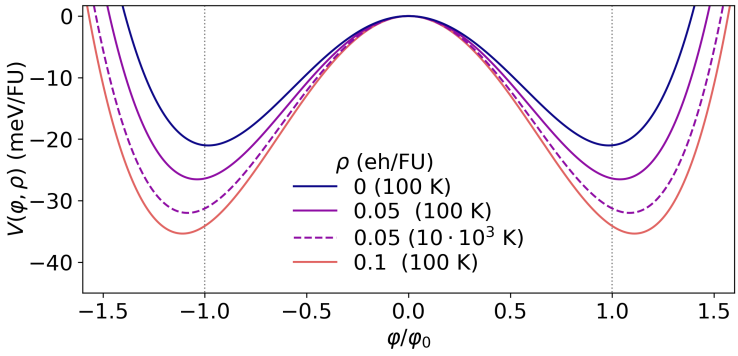

FIG. S5. Calculated potential of the AFD soft mode for two different carrier excess energies (represented by the temperature of the electronic system). The three solid lines correspond to an excess temperature of electrons and holes of 100 K at three different doping levels while the dashed line shows a select doping level for an electronic temperature of $10 \cdot 10^3$ K.

and by integration obtain the double well potential with respect to one individual oxygen site:

$$V_O(\varphi, \rho) = a(\rho)/2 \cdot \varphi^2 + b(\rho)/4 \cdot \varphi^4 \tag{2}$$

The coefficients $a(\rho)$ and $b(\rho)$ scale in good approximation linearly with ρ which allows us to interpolate $V(\varphi, \rho)$ for arbitrary doping levels. The potentials shown in Fig. 3 and Fig. S5 consider one formula unit (FU). Finally, we note that for $\rho = 0$ the corresponding soft-mode frequency is 3.9 THz and the minima of the double-well potential are at $\varphi_0 = \pm 6.3°$.

Ultrafast optical response of $EuTiO_3$ films

We investigate the transient reflectivity change $\Delta R(t)$ of $EuTiO_3$ in a supplementary optical pump/probe experiment using 80 fs pulses centred at a photon energy of 1.55 eV as pump and probe (Figure S6). The spot sizes of the pump and probe beams at the sample position are 525 μm and 190 μm, respectively. The sample is a 100 nm thin film of $EuTiO_3$ grown on a $SrTiO_3$ substrate under similar conditions as the 40 nm film used for the time-resolved X-ray studies. We observe a fast onset of $\Delta R(t)$ which is limited by the pump and probe pulse duration. The subsequent relaxation of the transient reflectivity change slows down with decreasing excitation fluence. This is a characteristic fingerprint of a band-to-band recombination process that behaves like a bimolecular carrier recombination process

for which the recombination rate is proportional to the squared density of electron hole pairs [13].

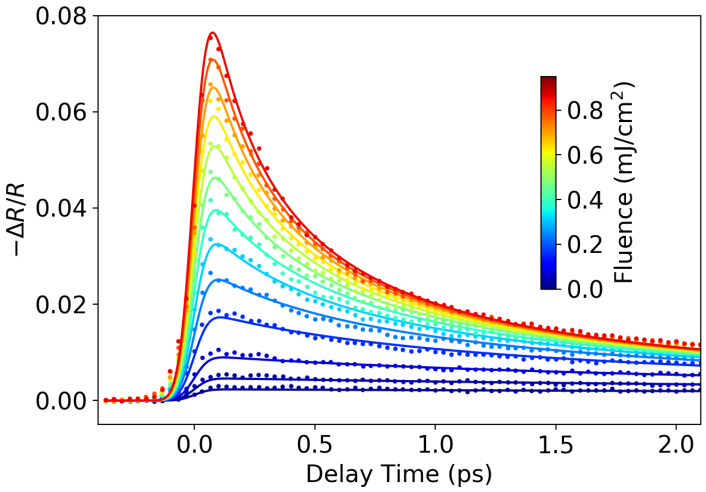

FIG. S6. Ultrafast reflectivity change $-\Delta R/R$, as a function of delay time, of a $EuTiO_3$ 100 nm thin film measured with 80 fs pulses at a central photon energy of $E_p = 1.55\,\mathrm{eV}$ and an angle of incidence of 10°. The different curves show excitation with the same photon energy with different excitation intensities. The base temperature is set to 120 K. Solid lines are derived from fitting the bimolecular decay model described in the text. The data and fit curves are color coded by the absorbed excitation fluence.

To test whether such a recombination dynamics can describe the transient reflectivity change, we assume the eh-density $\rho(t)$ to be given by

$$\dot{\rho} = -k_2\rho^2 + \frac{\rho_p}{\sqrt{2\pi\tau_p^2}} \exp\left[-0.5(t/\tau_p)^2\right] \tag{3}$$

where the first term describes the density dependent recombination rate and the second term the photogeneration of a carrier density ρ_p by a pump pulse of duration τ_p. Assuming that $\Delta R(t)$ is proportional to $\rho(t)$, we fit equation (3) to the experimental data leaving the proportionality constant as a fit parameter. Thereby we simultaneously adapt the model to the data taken at different excitation fluences by setting ρ_p for the individual model curves to the value set by the experimental conditions (see Methods). After accounting for the time resolution given by the probe pulse duration, we obtain the solid lines in Fig. S6. The model fit describes the slow down with decreasing fluence correctly (with $k_2 = 5 \cdot 10^{-9}\mathrm{s}^{-1}\mathrm{cm}^3$) and is in reasonable agreement with the experimental data.

As nonequilibrium optical properties for photon energies above the band gap also depend on the temperature of the electronic system, we next test whether the transient optical response of the free carrier system is compatible with a carrier recombination process. To this end, we monitor the ultrafast optical response of the 100 nm $EuTiO_3$ film in the multi-THz regime. We thereby restrict the studied spectral range of the reflectivity change to frequencies above the phonon reststrahlen band of $EuTiO_3$ which has its highest LO phonon frequency at 25 THz [14]. This ensures that the probed transient reflectivity change mainly originates from the photoinduced Drude conductivity [15, 16], as resonances of quasiparticles in this spectral range, such as intraexcitonic transitions, are not expected under the intense excitation conditions used in our studies.

We photoexcite with 12-fs pulses centred at a photon energy 1.55 eV and subsequently probe the reflectivity with few-cycle ultrabroadband THz pulses which are recorded with electro-optic sampling. To obtain a peak excitation intensity of $1.3\,\mathrm{mJ/cm^2}$ with the laser system used for this study [16], the spot size of the pump focus was set to $30\,\mu$m (FWHM), which is smaller than the size of the THz probe spot of $\approx 40\,\mu$m (FWHM). Fourier transformation of the acquired THz waveforms allows us to derive the transient field reflection coefficient r as a function of the THz probe frequency and pump-probe delay time [15, 16]. Figure S7 shows the obtained relative change of $r(t)$ averaged in a frequency window of 28 to 35 THz. We find a decay of $r(t)$ qualitatively similar to the dynamics observed in the near-infrared pump-probe study for the highest fluence tested. As the photoinduced change of $r(t)$ depends mainly on the Drude response of photoinjected free carriers in the $EuTiO_3$ film, its decay is consistent with a reduction of the free carrier density via recombination.

Details on the structural dynamics model

To describe the dynamics of the octahedral rotation we start with the equation of motion for one oxygen site along the soft-mode coordinate given by

$$m_O\ddot{u} + 2\gamma\dot{u} + \frac{\partial}{\partial u}V_O(u(t), \rho_{eff}(t)) = 0. \tag{4}$$

u denotes the atomic displacement of an oxygen at the $8h$ position along the octahedra rotation (note that $u \propto \varphi$ to first order [16]), γ is the damping and m_O represents the oxygen atomic mass. To model the heating-induced relaxation of the double-well potential,

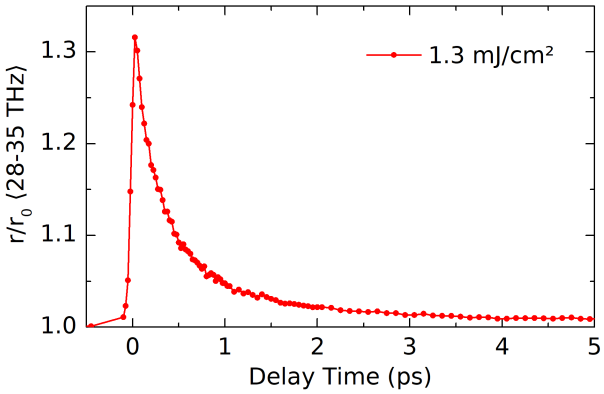

FIG. S7. Transient field amplitude reflection coefficient $r(t)$ of a 100 nm thin $EuTiO_3$ film averaged in a multi-THz spectral window above the phonon reststrahlen band. The dynamics is induced by 12-fs excitation pulses with a central photon energy of = 1.55 eV). $r(t)$ probes the recombination dynamics of the photoexcited eh pairs.

we extrapolate V along its dependency on ρ towards the high-symmetry phase. For that we introduce and effective doping

$$\rho_{\text{eff}}(t) = \rho(t) - \left(c_1 \cdot \int_{-\infty}^{t} k_2 \cdot \rho(t')^2 \mathrm{d}t' \right)^{c_2} \tag{5}$$

that make V dependent on the transient doping level $\rho(t)$ as described by equation (3). This creates a phenomenological measure for accumulated heat in the phonon system at the time t, that includes the time integrated eh recombination rate.

By solving equation (4) for $u(t)$, we can now fit this model to the normalized transient superlattice scattering intensity with ρ_p, c_1, c_2 and k_2 as free fit parameters. Thereby we account for the experimental time-resolution set by the X-ray pulse duration and time-binning. The value of γ is phenomenologically fixed corresponding to a coherent lifetime of the soft-mode of 0.14 ps. Independent of the excitation conditions, the fit yields $c_2 = 6 \cdot 10^{-1}$ and $k_2 = 2 \cdot 10^{-9} \mathrm{s}^{-1} \mathrm{cm}^3$.

As the phenomenological parameters in the model describe the decay dynamics, they have little influence on the initial rise of the enhanced rotation which is mainly governed by ρ_p. This allows for quantitative comparison of ρ_p obtained by the model fit to the values set in the experiment:

For excitation with 1.55 eV photons and 3.86 $\mathrm{mJ/cm}^2$ absorbed fluence, we estimate a doping level of 0.23 eh/FU in the experiment. This coincides well with $\rho_p = 0.25$ eh/FU obtained

from the fit. With increased carrier excess energy by excitation with 3.1 eV photons at $3.86\,\mathrm{mJ/cm^2}$ we estimate a doping of 0.11 eh/FU in the experiment while we obtain $\rho_p = 0.17\,\mathrm{eh/FU}$ from fitting the model. As discussed in the main text, we observe that doubling the excess energy results in an only slightly reduced maximum enhancement of the rotation angle at approximately half the number of injected eh pairs. While our DFT calculations reproduce (Fig. S5) this experimentally observed trend, we do not include the electronic excess energy/electronic temperature into the dynamics model. This likely explains the higher value of ρ_p needed to reproduce the experimental results.

We fit the model to the data shown in Fig. 2 for all fluences simultaneously while keeping the ratio of the doping parameters ρ_p to the experimentally set conditions.

[1] S. Herrmann, S. Boutet, B. Duda, D. Fritz, G. Haller, P. Hart, R. Herbst, C. Kenney, H. Lemke, M. Messerschmidt, J. Pines, A. Robert, M. Sikorski, and G. Williams, Nuclear Instruments and Methods in Physics Research Section A: Accelerators, Spectrometers, Detectors and Associated Equipment Proceedings of the 12th Pisa Meeting on Advanced Detectors, **718**, 550 (2013).

[2] M. R. Bionta, N. Hartmann, M. Weaver, D. French, D. J. Nicholson, J. P. Cryan, J. M. Glownia, K. Baker, C. Bostedt, M. Chollet, Y. Ding, D. M. Fritz, A. R. Fry, D. J. Kane, J. Krzywinski, H. T. Lemke, M. Messerschmidt, S. Schorb, D. Zhu, W. E. White, and R. N. Coffee, Review of Scientific Instruments **85**, 083116 (2014).

[3] J. H. Lee, X. Ke, N. J. Podraza, L. F. Kourkoutis, T. Heeg, M. Roeckerath, J. W. Freeland, C. J. Fennie, J. Schubert, D. A. Muller, P. Schiffer, and D. G. Schlom, Applied Physics Letters **94**, 212509 (2009).

[4] S. Zollner, A. A. Demkov, R. Liu, P. L. Fejes, R. B. Gregory, P. Alluri, J. A. Curless, Z. Yu, J. Ramdani, R. Droopad, T. E. Tiwald, J. N. Hilfiker, and J. A. Woollam, Journal of Vacuum Science & Technology B: Microelectronics and Nanometer Structures Processing, Measurement, and Phenomena **18**, 2242 (2000).

[5] L. A. A. Pettersson, L. S. Roman, and O. Inganäs, Journal of Applied Physics **86**, 487 (1999).

[6] M. Porer, M. Fechner, E. M. Bothschafter, L. Rettig, M. Savoini, V. Esposito, J. Rittmann, M. Kubli, M. J. Neugebauer, E. Abreu, T. Kubacka, T. Huber, G. Lantz, S. Parchenko,

S. Grübel, A. Paarmann, J. Noack, P. Beaud, G. Ingold, U. Aschauer, S. L. Johnson, and U. Staub, Physical Review Letters **121**, 055701 (2018).

[7] The Elk LAPW Code. http://elk.sourceforge.net.

[8] J. P. Perdew, A. Ruzsinszky, G. I. Csonka, O. A. Vydrov, G. E. Scuseria, L. A. Constantin, X. Zhou, and K. Burke, Phys. Rev. Lett. **100**, 136406 (2008).

[9] T. Birol and C. J. Fennie, Physical Review B **88** (2013), 10.1103/physrevb.88.094103.

[10] J. L. Bettis, M.-H. Whangbo, J. Köhler, A. Bussmann-Holder, and A. R. Bishop, Phys. Rev. B **84** (2011), 10.1103/physrevb.84.184114.

[11] P. Tangney and S. Fahy, Physical Review Letters **82**, 4340 (1999).

[12] D. M. Fritz, D. A. Reis, B. Adams, R. A. Akre, J. Arthur, C. Blome, P. H. Bucksbaum, A. L. Cavalieri, S. Engemann, S. Fahy, R. W. Falcone, P. H. Fuoss, K. J. Gaffney, M. J. George, J. Hajdu, M. P. Hertlein, P. B. Hillyard, M. H.-v. Hoegen, M. Kammler, J. Kaspar, R. Kienberger, P. Krejcik, S. H. Lee, A. M. Lindenberg, B. McFarland, D. Meyer, T. Montagne, E. D. Murray, A. J. Nelson, M. Nicoul, R. Pahl, J. Rudati, H. Schlarb, D. P. Siddons, K. Sokolowski-Tinten, T. Tschentscher, D. von der Linde, and J. B. Hastings, Science **315**, 633 (2007).

[13] U. Strauss, W. W. Rühle, and K. Köhler, Applied Physics Letters **62**, 55 (1993).

[14] M. Kachlik, K. Maca, V. Goian, and S. Kamba, Materials Letters **74**, 16 (2012).

[15] R. Huber, F. Tauser, A. Brodschelm, M. Bichler, G. Abstreiter, and A. Leitenstorfer, Nature **414**, 286 (2001).

[16] M. Porer, U. Leierseder, J.-M. Ménard, H. Dachraoui, L. Mouchliadis, I. E. Perakis, U. Heinzmann, J. Demsar, K. Rossnagel, and R. Huber, Nature Materials **13**, 857 (2014).